

Article

Potential Benefits of Combining Anomaly Detection with View Planning for UAV Infrastructure Modeling

R. Abraham Martin ¹, Landen Blackburn ¹, Joshua Pulsipher ¹, Kevin Franke ² and John D. Hedengren ^{1*}

¹ Dept. of Chemical Engrg., Ira A. Fulton College of Engrg. and Technology, Brigham Young University, 350 Clyde Building, Provo, UT 84602, USA

² Dept. of Civil and Env. Engrg., Ira A. Fulton College of Engrg. and Technology, Brigham Young University, 368 Clyde Building, Provo, UT 84602, USA

* Correspondence: john.hedengren@byu.edu; Tel.: +1-801-477-7341

Academic Editor: name

Version April 20, 2017 submitted to Remote Sens.

Abstract: This paper presents a novel method for UAV based 3D modeling of large infrastructure objects such as pipelines, canals, and levees that combines anomaly detection with automatic on-board 3D view planning. The study begins by assuming that anomaly detections are possible, and focuses on quantifying the potential benefits of the combined method and the view planning algorithm. A simulated canal environment is constructed, and several simulated anomalies are created and marked. The algorithm is used to plan inspection flights for the anomaly locations, and simulated images from the flights are rendered and processed to construct 3D models of the locations of interest. The new flights are compared to traditional flights in terms of flight time, data collected, and 3D model accuracy. When compared to a low speed, low elevation traditional flight, the proposed method is shown in simulation to decrease total flight time by up to 55% while reducing the amount of image data to be processed by 89% and maintaining 3D model accuracy at areas of interest.

Keywords: UAV; infrastructure monitoring; structure-from-motion; view planning; intrusion detection

1. Introduction

The advent of small Unmanned Aerial Systems (sUAS) has given rise to a host of new applications for aerial imaging technology in many fields [1–5]. Together with the increasing ease of obtaining imagery, advances in computer vision and computer processing power have led to a widespread increase in aerial mapping and 3D-reconstruction [6–8]. In the field of infrastructure monitoring, the clear advantages of on-demand, high precision 3D modeling are driving companies and researchers to explore the possibilities of this technology (for an excellent overview, see [9]). However, current UAV and 3D reconstruction technology still has limitations. While excellent results can be obtained for single site projects as demonstrated by [10], UAV flight time, computational power, data storage, and model processing time all constrain the scalability of this technology to large scale infrastructure systems such as pipelines, canals, levees, railroads, utility lines and other long linear features ([11]). Because of these constraints, creating a single detailed 3D model of a large infrastructure object is in many cases impractical.

In this paper, the authors attempt to address some of these limitations by introducing a concept in which a single UAV platform serves as a multi-scale monitoring system. The UAV first inspects the structure at a relatively high level, collecting imagery and searching for potential anomalies. A detection triggers a 3D flight planning algorithm that updates the UAV path to collect additional

31 images of the detection area. This allows the area of interest to be reconstructed at a higher level of
32 detail than would be possible in the baseline survey. This multi-scale monitoring concept focuses flight
33 time and computational resources on areas of the infrastructure with high information content.

34 Although there is a large body of work relating to UAVs tracking moving objects and real-time
35 detection of specific objects, real-time detection of unknown anomalies is a challenging problem, and
36 this paper does not attempt to address it directly. See [12], [13], [14], [15], [16], and [17]. Many possible
37 approaches to detection are possible, including cascade classifiers, neural networks or change detection
38 between monitoring flights and a known baseline data set ([18]). The approach could also be expanded
39 to other sensors such as multispectral or hyperspectral sensors, real-time stereo, LiDAR, chemical
40 sniffers, or any other sensor capable of detecting the desired anomalies. The body of the work proceeds
41 on the assumption that accurate detections can be made, and the focus is placed on the potential
42 benefits of a multi-scale approach in terms of model accuracy, flight time and data quantity, with the
43 goal of motivating further work in real-time detection technology and algorithms.

44 *1.1. Related Work in Linear Feature Monitoring*

45 Although the use of UAV technology in civil applications is a relatively new field, a number of
46 authors have explored various aspects of monitoring long linear infrastructure with UAVs. [19] analyze
47 a wide variety of UAV platforms and sensors subject to the application infrastructure inspection. They
48 comment on what is currently available "off the shelf" to gather optical data of infrastructure using
49 relatively low cost UAV systems. They also conduct a test case using a small quadrotor UAV to inspect
50 a section of railroad tracks. [20] consider two possible UAV systems for the inspection of natural gas
51 pipelines. The first system, a low altitude, small UAV with visual sensors, is most similar to the UAV
52 platform considered in the current work. Portions of the system are demonstrated, including automatic
53 detection and marking of areas of concern. The authors conclude that although a lack of operation
54 standards impedes immediate adoption of the technology, the system is technologically feasible in this
55 application.

56 In another application, [21] study the high speed inspection of power lines using UAVs.
57 Their focus is primarily on automatic detection and tracking of the lines in video. [22] detail the
58 implementation of an algorithm that utilizes optical imagery to guide a small UAV along long
59 linear infrastructure such as canals, roads, and pipelines without the use of GPS waypoints. Several
60 experiments were conducted that demonstrated the effectiveness of the algorithm in navigating a
61 small UAV over canals and roads to collect optical imagery. They conclude that small UAVs can gather
62 a large amount of optical data of long linear sites in a relatively short period of time.

63 [23] propose a navigational framework to detect and track road networks. They were able to
64 demonstrate via simulation that their framework could be used to navigate a UAV over long stretches of
65 road for the purpose of visual inspection. The current work extends upon these studies by considering
66 the case of a UAV platform that not only passively monitors infrastructure, but actively re-plans its
67 flight path using optimized view planning when anomalies are detected.

68 *1.2. Optimized View Planning*

69 [24] defines view planning as the strategic placement of sensor(s) to gather desired information
70 about an object or scene. The origins of view planning are discussed by [25]. View planning has
71 its earliest roots in the "art gallery" problem, where one desires to place security guards in optimal
72 locations to monitor an art gallery. [26] examine how view planning has also been used in quality
73 control, where ideal locations for sensors are desired to ensure product quality in manufacturing.

74 Modern examples of view planning often utilize remote optical sensors, and the placement
75 is typically automated by robotic arms, gimbals, and unmanned aerial vehicles. [27] describe a
76 step-by-step process for automating the surveillance of a construction site with a UAV, with an
77 emphasis on the UAV's ability to easily survey areas that pose significant danger to human operators.
78 A simple grid pattern or 'lawnmower' pathway is used at a set altitude, with the UAV constructing

79 an orthophoto from images taken exclusively in the nadir position. The lawnmower pathway is
80 commonly used in UAV applications due to its simplicity and even coverage.

81 The view planning problem is described by [28] as NP-complete, which is the most difficult subset
82 of problems. The NP-complete class of problems is characterized by having an easy method to check if
83 solutions are correct, but having no known algorithm for efficiently generating solutions.

84 Work by [29] shows the difficulty of the viewing problem. Saadat and Samadzadegan use a
85 genetic algorithm to create a Pareto front where multiple optimized viewing networks are generated.
86 However, an experienced operator is then needed to select which one is anticipated to result in a
87 superior network.

88 [30] emphasize the need to generate view planning solutions for UAVs that give the best results
89 given constraints, such as flight time or battery life of the UAV. They address the situation of a UAV
90 tasked with surveying more infrastructure objects than can be visited within a single battery charge.
91 A weighted objective function is used that assigns rewards for exploring unknown area as well as
92 inspecting certain points that are deemed more important. The authors use a simple heuristic approach
93 to connect the waypoints, solving the Traveling Salesman Problem with an approximation. Their
94 overall method yielded good results in real time, even though sub-optimal heuristic approaches were
95 used.

96 The work of [31] presents an algorithm for efficiently generating potential view points then
97 heuristically selecting the view points that best contribute to network strength. The flight planning
98 method presented in the current work builds upon the algorithm developed by Hoppe et al. Their
99 method is extended from known 3D structures to unknown objects located on potentially flat surfaces.
100 The new algorithm presented is also configured to be called in real-time by the UAV during flight to
101 re-plan the mission based on updated information.

102 1.3. Simulation

103 Experiments for this paper are performed in both a terrain simulation environment and a
104 software-in-the-loop flight simulator. This approach is relatively novel in this field, but it has been
105 demonstrated in some capacity before [32]. In one example of a similar approach, [33] develop a
106 simple 3D environment for use in photogrammetric simulations. They demonstrate a process for
107 reconstructing perspective imagery from their scenes with user specified camera parameters. While
108 some mission planning capabilities are also shown, the scene geometry is limited to simple shapes,
109 and the software package is developed primarily as a learning tool for students. [34] also use a
110 simple 3D simulation, though in this case the objective is to evaluate the effects of various UAV image
111 configurations on the systematic error in the resulting DEM.

112 Although uncommon to this point in civilian applications, the simulation of UAV surveillance
113 flights using synthetic imagery generated by military simulation packages has also been explored.
114 In particular, the simulation environment Virtual Battle Space 3 has been used by [35] to perform
115 experiments in the context of a UAV road monitoring and change detection problem. The authors
116 concluded that although some artifacts were introduced by the rendering process, the resulting images
117 were of sufficient fidelity to evaluate their computer vision algorithms.

118 Terragen 3, the environmental simulator used in the current work, has been used successfully
119 by the authors in a previous paper in which it was used to evaluate the performance of a genetic
120 algorithm based planner for UAV infrastructure modeling ([36]). This approach differs from related
121 work in the field through an increased level of fidelity in the simulation environment, including highly
122 detailed vegetation models, realistic atmospheric effects, cloud cover, haze, and fine control of camera,
123 lens, and lighting conditions. This allows for simulations more closely approximating actual field
124 conditions, and increases the amount and quality of testing that can be performed prior to physical
125 flight tests.

126 1.4. Novel Contributions and Paper Overview

127 This paper advances the state of the art in the following areas.

- 128 • It is shown that when a reliable anomaly detection system becomes available, the proposed
129 method will be capable of generating detailed 3D models of the areas of interest while avoiding
130 the often unwieldy amounts of data produced by repeatedly creating 3D models of the entire
131 structure in routine inspections.
- 132 • The monitoring system incorporates on demand optimized view planning, taking advantage of
133 the onboard processing capabilities of unmanned aircraft to maximize information gain through
134 in-flight re-planning.
- 135 • The potential benefits of this method are demonstrated and quantified in simulation, motivating
136 further work on the supporting automatic detection technologies.

137 The paper begins with an overview of the simulation environment used to perform the
138 experiments described in the paper. This is followed by an explanation of both the standard linear and
139 the optimized flight paths used for generating synthetic UAV images in the simulation environment.
140 The process of 3D model creation and accuracy testing is described, as is the configuration of the
141 real-time simulated flight testing system. The results of the testing for 3D model accuracy, flight
142 time, and data quantity are then presented, and the implications of the results are summarized and
143 discussed.

144 2. Methods

145 2.1. Simulated Test Scene

146 Synthetic images for this study are generated using the terrain simulation environment Terragen
147 3. The simulated scene is based on 0.5 meter elevation data taken from a one mile section of canal
148 near Payson Utah. Satellite imagery at 12.5 cm resolution is overlaid on the elevation data, and high
149 quality 3D vegetation and trees are added to approximate the actual environment at the site. Lighting
150 conditions and the position of the sun are chosen to match those for Payson, Utah on March 28th, 2016
151 at 12:00 p.m. Figure 1 shows a portion of the completed simulation site.

152 In order to simulate a wide variety of potential infrastructure anomalies, additional 3D objects are
153 introduced into the scene and placed at intervals along the canal. These included a set of power lines
154 with structural damage, a colored disc placed on a road, a section of industrial piping with horizontal
155 displacement, and short segment of railroad with a tie out of place. A slump in the side of the canal is
156 also simulated by displacing a portion of the canal bank and filling the vacant area with water. Each
157 anomaly in this study is a displacement on the order of 50 cm from a baseline case. A full description
158 of the exact nature of the anomalies is not given here, as the purpose of the anomalies in this paper is
159 only to illustrate potential locations where they could be found. A follow-up study will investigate
160 the specific types of anomalies that can be detected, and quantify the limitations of the method with
161 regards to anomaly size. Closeups of four of the anomaly locations can be seen in Figure 2.

162 Terragen 3 permits full control over camera positioning, orientation, and parameters. Camera
163 parameters for this study are chosen to simulate a Nikon D7100 DSLR camera, and are detailed in
164 Table 1.

165 While the simulation engine used is capable of generating photo-realistic images, it is not a perfect
166 representation of reality. In particular the effects of wind on the scene and the rolling shutter effect due
167 to camera movement are not accounted for. These effects are important in UAV photogrammetry, and
168 including them in a simulation environment would be an interesting area of future work.

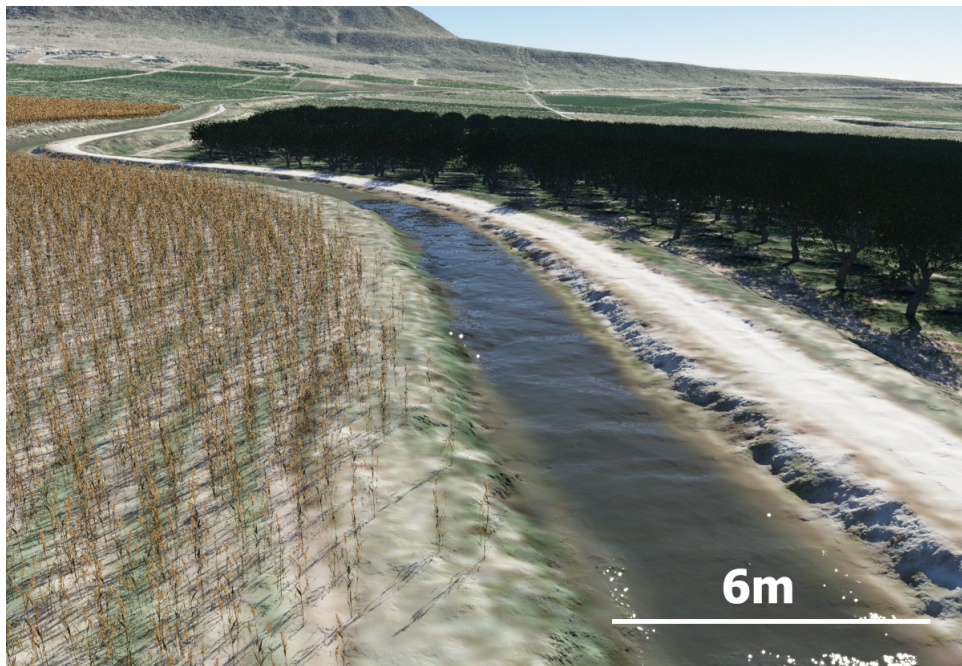


Figure 1. Simulation of the Highline Canal near Payson, Utah

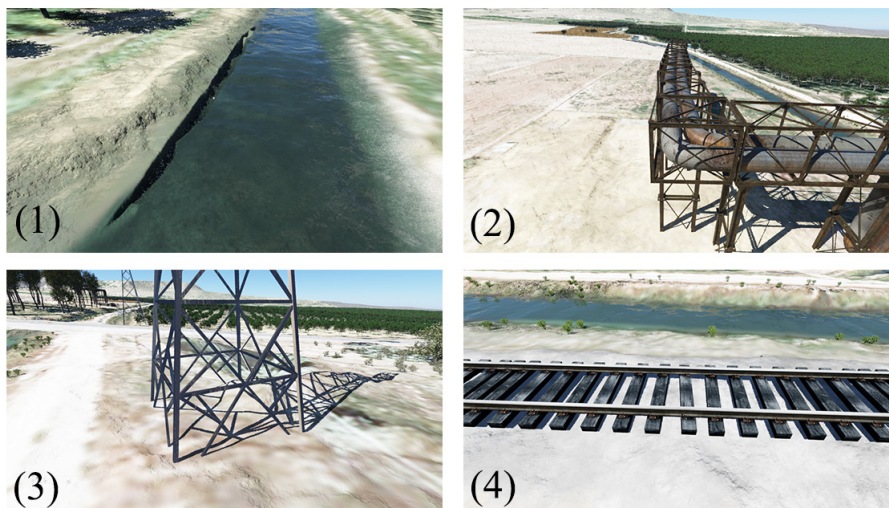


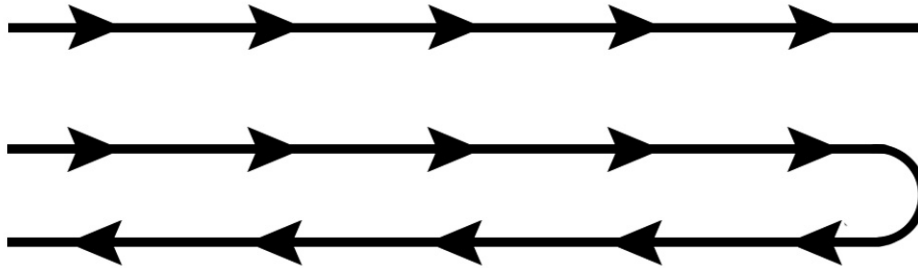
Figure 2. Closeup views of anomaly locations. (1) Canal Slump, (2) Industrial Piping, (3) Power Line, (4) Railway.

Table 1. Camera settings for image generation.

Setting	Value
Sensor Width (mm)	23.5
Focal Length (mm)	35
Image Width (pixels)	6000
Image Height (pixels)	4000

169 2.2. Standard Path Planning

170 To facilitate comparison with standard flights, a planner is created to generate flight paths along
 171 the canal. Given a vehicle speed, desired image overlap, and camera frame rate, the planner generates a
 172 sequence of image locations at the required spacing and elevation. The planner is capable of generating
 173 single track paths, in which the UAV flies only one direction, as well as double track, in which the
 174 UAV flies down and back. This is illustrated in Figure 3. In the case of the double track path, the side
 175 overlap between the two tracks can also be specified.

**Figure 3.** Illustration of single track (above) and double track (below) UAV flight paths

176 Image locations are generated for a range of flight speeds between 20 and 60 mph, and image
 177 overlaps between 75% and 90%. Double track flight paths are also generated, with a 50% overlap
 178 between the tracks. These ranges were based on commonly used corridor mapping guidelines [37].
 179 All paths are created using a fixed camera frame rate of 0.5 frames per second.

180 The required elevation and number of images for each path generated by the standard path
 181 planner are shown in Tables 2 and 3.

Table 2. Standard Path Planner: Single Path Results

Case #	Speed (mph)	Overlap (%)	# of Images	Elevation (m)	GSD (cm)
1	20	75	193	84	0.94
2	60	75	65	252	2.8
3	20	90	193	210	2.3
4	60	90	65	630	7.1

Table 3. Standard Path Planner: Double Path Results

Case #	Speed (mph)	Overlap (%)	# of Images	Elevation (m)	GSD (cm)
5	20	75	392	84	0.94
6	60	75	137	252	2.8
7	20	90	403	210	2.3
8	60	90	158	630	7.1

182 Because the camera frame rate has been fixed at 0.5 frames per second in this study, some
183 combinations of speed and image overlap produce a very high elevation requirement. These elevations
184 are outside the typical operating range of a small UAV, but are included for completeness.

185 2.3. *Optimized 3D Flight Path Planning*

186 Calculations that result in the global optimum for view planning are difficult to formulate and
187 lead to very expensive computational loads. The view planning algorithm developed in this paper
188 therefore focuses on identifying a sub-optimal solution capable of producing desirable results with
189 a computational load that permits near real time calculations. The algorithm includes high degree
190 of adaptability to different UAV platforms and desired image resolutions by accepting several user
191 specified parameters that define the capabilities of the camera and desired resolution. Given these
192 parameters, the algorithm estimates the minimal set of camera locations required for 3D reconstruction,
193 as well as the optimal order in which to visit them. For a typical site of interest (about 900 m²), the
194 algorithm finds acceptable image positions and a near optimal route through those points in about
195 0.65 seconds on an Intel I7 CPU with 16 GB of RAM.

196 As it is desirable for the algorithm to eventually run on-board a UAV, the algorithm is also tested
197 on a Raspberry Pi 3. The Pi 3 is a small, single board computer with a 1.2 GHz 64-bit quad-core ARMv8
198 CPU, and 1 GB of RAM. The board measures 85.60mm x 56.5mm and weighs 45g, which makes it
199 feasible for use on-board a UAV. Running on the Raspberry Pi 3, the algorithm took an average of 7.02
200 seconds to compute both the image positions and route for the five test areas in the study, placing it
201 within range of in flight re-planning.

202 The view planning algorithm can be summarized as follows:

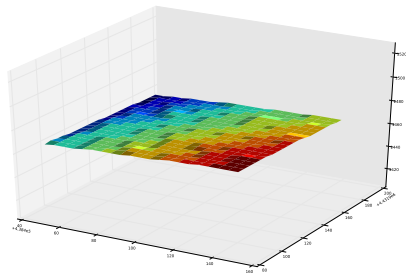
- 203 1. Receive detected anomaly location
- 204 2. Obtain a point-cloud
- 205 3. Add dome projection at the point of interest
- 206 4. Convert the point-cloud terrain into a triangle mesh
- 207 5. Place an aerial camera location on the normal line of every triangle
- 208 6. Remove underground and blocked images
- 209 7. Select the best images from the group based on a set of value heuristics
- 210 8. Find the shortest path through all these points

211 The following is a description of each of the above steps. Elevation data for the area to be
212 surveyed is downloaded prior to the flight from public data sources, such as the USGS National
213 Elevation Dataset. During an actual UAV flight, points of interest are flagged by anomaly detection;
214 however, for the purposes of this paper, the points of interest are manually tagged before the simulated
215 flight begins. When a point is detected, a geometric area of interest is constructed around the point to
216 define the area to be inspected.

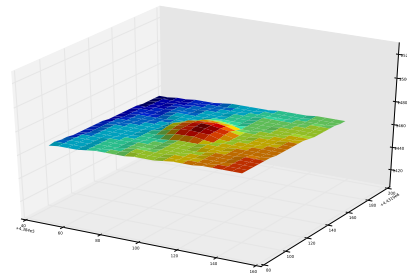
217 After identifying the area of interest, the full elevation data set is trimmed down to an area only
218 slightly larger than the area of interest. The slight excess of data is retained to ensure the UAV remains
219 safe from potential obstacles or obstructions. Using only a subset of the original data also greatly helps
220 to minimize computational costs when determining which points are within the view of each camera.

221 In many cases, the geometry of the detected anomaly is unknown, and is not included in the
222 available elevation data. This can lead to insufficient oblique imagery of the anomaly, especially if the
223 shape of the anomaly differs significantly from the underlying terrain. To improve coverage, when
224 an anomaly is detected the algorithm automatically inserts a dome projection at the point of interest,
225 as demonstrated in Figure 4. The authors have found that the addition of the dome into the dataset
226 aids the algorithm in selecting sufficient oblique imagery to capture the sides of an unknown object,
227 regardless of whether the object is on relatively flat ground or on a steep grade. The dome is created
228 by translating the elevation of each data point upward using a spherical cap, which results in a dome
229 shape that still maintains the underlying geometry of the surface. Without the dome, a flat surface
230 would result in the camera set all pointing directly downwards and the resulting 3D reconstruction

231 could yield undesirable results. The authors have found that a dome height of 5-10 meters and an
 232 incident angle with the horizontal of $15\text{-}30^\circ$ provide an optimal increase in coverage. If the approximate
 233 size of the anomaly is known, it is best that the dome is tall and wide enough to completely enclose
 234 the anomaly. In the case that additional information is available about the nature of the anomaly, that
 235 information should be used in the planning rather than the generic dome projection. To clarify, the
 236 dome is not inserted into the Terragen simulation, it is only used in the view planning algorithm to aid
 237 in selecting imaging locations.

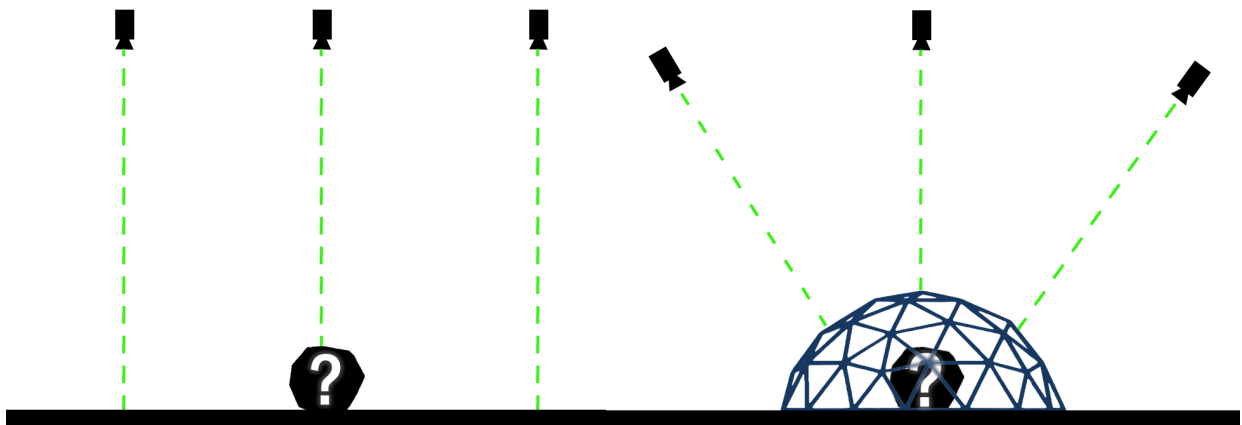


(a) Terrain without dome projection.



(b) Terrain with dome projection.

Figure 4. Dome projection inserted to account for unknown anomaly shape.



(a) Selected camera positions with no added dome.

(b) Selected camera positions with added dome.

Figure 6. The added dome projection helps guide the algorithm to capture additional oblique imagery of an anomaly with unknown geometry.

238 This resulting elevation data is then converted to a triangle mesh, and the triangle size is
 239 normalized by recursive subdivision. This ensures even coverage of vertical features such as cliffs,
 240 hills, and canyons, even though the original telemetry data is spaced evenly for latitude and longitude.

241 After creating the triangle mesh and adjusting the terrain, tentative camera locations are generated
 242 at a fixed distance from each triangle midpoint along the normal from each surface. This typically
 243 results in several thousand tentative camera locations. Potential camera locations that are generated
 244 underground or are otherwise blocked from viewing their original triangle midpoints are removed.

245 The image selection criteria is based on minimizing the total number of images while maximizing
 246 the terrain coverage. A visibility matrix similar to the 3M matrix used by [38] is constructed, containing
 247 information on the visibility of each point in the terrain from each camera location, and the angles
 248 (relative to each surface's normal) at which each point is viewed. The angles are divided into three
 249 ranges (see Figure 8) and the resulting range is recorded in the histogram. An iterative process then
 250 selects camera locations which maximize the number of triangle midpoints viewed from previously
 251 unused angles. That is, once a point is viewed from an angle range, it is considered viewed, and it no
 252 longer contributes to the value of other camera locations which view it from within the same angle
 253 range. This results in a sub-optimal heuristic algorithm which, while not guaranteed to be optimal, can
 254 be completed very quickly with satisfactory results. As noted in [39], this type of heuristic algorithm
 255 provides a $(1 + \ln n)$ approximation, where n is the number of images in the optimal solution.

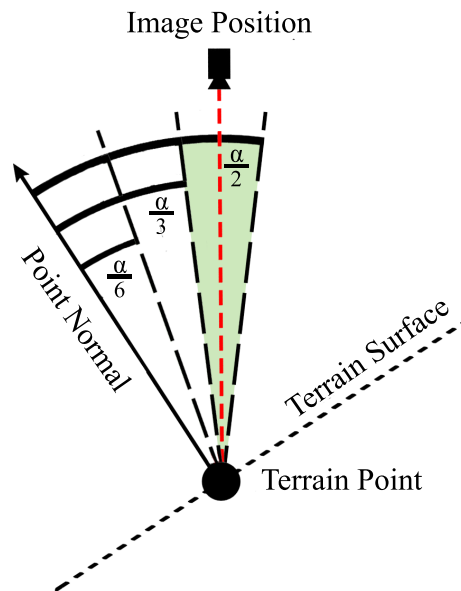


Figure 8. Angle ranges for histogram, where α is the camera angle of view.

256 Once the optimal images are chosen, a short route must be planned for the UAV to visit all the
 257 points; this is an example of a 3D Traveling Salesman problem. To find a solution, the Christophides
 258 Algorithm is employed. This algorithm is an approximation, but is guaranteed to find a solution
 259 within 1.5 times the length of the optimal solution ([40]). For this application, it was observed that the
 260 Christophides algorithm typically generates solutions that are within 10% of the optimal length as
 261 computed by integer linear programming, as shown in Equations 1-3.

$$\text{minimize } \sum_{i=1}^k \sum_{j=1}^k D_{i,j} * x_{i,j} \quad (1)$$

262 Here each of the k waypoints is numbered from 1 to k , and i and j represent the waypoints at either
 263 end of a selected pathway. D contains the distance measurements between each of the waypoints. The
 264 end solution x contains integers bounded between 0 and 1.

265 The equality constraints are shown in Equation 2 and the inequality constraints are shown in
 266 Equation 3.

$$\sum_{i=1}^k \sum_{j=1}^k x_{i,j} = k \quad (2a)$$

$$\text{for } j \text{ in range } \{1\dots k\} : \sum_{i=1}^k x_{i,j} = 2 \quad (2b)$$

267 If a solution is achieved with subtours, Equation 3 is added as an inequality constraint and the
268 problem is solved again. The variable s represents a subtour that occurred in a previous solution.

$$\sum_{i=1}^k \sum_{j=1}^k s_{i,j} * x_{i,j} <= \sum_{i=1}^k \sum_{j=1}^k s_{i,j} - 1 \quad (3)$$

269 A sample comparison between the Christophides solution and the optimal solution from linear
270 programming can be found in Table 4. A completed solution for a generic anomaly, including selected
271 camera locations and the shortest flight path can be found in Figure 9. For comparison, Figure 9 also
272 shows the optimal solution when the dome projection is not used.

Table 4. Christophides Algorithm Performance

Christophides (m)	Optimal (m)	Difference (%)
1270.2	1202.9	5.59 %
998.6	918.8	8.69 %
851.4	800.8	6.31 %
678.8	634.6	6.96 %
205.1	189.4	8.31 %

273 For comparison with Tables 2 and 3, the number of images taken by the optimized path planner
274 at each anomaly location as well as the average elevations of the images are shown in Table 5.

Table 5. Optimized Path Planner Results

Anomaly	# of Images	Average Image Elevation (m)
Power Line	14	90.2
Road Disc	14	91.0
Piping	58	86.0
Railway	19	85.4
Canal Slump	23	84.8

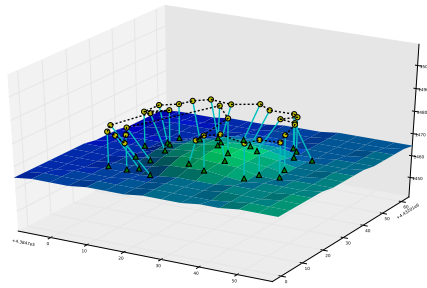
275 The number of images required to model the section of industrial piping is significantly larger
276 than the other anomaly areas. This can be explained by the fact that this anomaly location has the
277 largest area of the five due to the fact that it contains the largest structure.

278 2.4. 3D Modeling

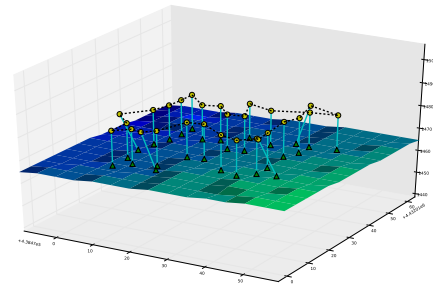
279 The synthetic imagery from the terrain simulation environment is processed to created 3D point
280 cloud models in the software package Agisoft Photoscan ([41]). No ground control points are used in
281 processing the models, and the software is allowed to self-calibrate all camera parameters. An example
282 of one of the 3D models generated is shown in Figure 12. The program settings used to generate the
283 models are detailed in Table 6.

284 2.5. 3D Accuracy Testing

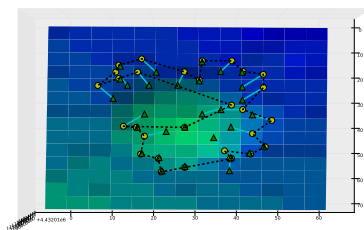
285 For each flight case in Tables 2 and 3, the accuracy of the 3D model is measured at each of the five
286 anomaly locations. Similar measurements are performed for the optimized case. The accuracy of the
287 3D models is evaluated by comparing against a ground truth point cloud created by exporting the



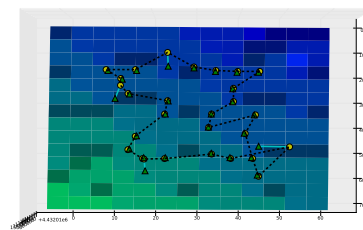
(a) Optimized flight plan with dome projection.



(b) Optimized flight plan without dome projection.



(c) Top down view of (a).



(d) Top down view of (b).

Figure 9. Example of an optimized camera view plan and flight path for a generic anomaly with and without the added dome projection. Yellow circles represent image locations, green triangles are corresponding image targets.

Table 6. Program settings for model reconstruction

Setting	Value
Photo alignment	High
Pair preselection	Generic
Key point limit	100,000,000
Tie point limit	10,000
Dense cloud quality	High
Depth filtering	Mild

288 original geometry of the scene from Terragen. This includes terrain, vegetation, and 3D objects, and
 289 preserves the scale of the scene. The geometry is exported as a 3D mesh, and is then sampled at a high
 290 density to create a point cloud.

291 Each model is evaluated for accuracy against the ground truth model using the techniques
 292 described in [36]. The models are aligned to the ground truth data set using the open source software
 293 package CloudCompare ([42]). This alignment is done in 2 parts. The first is to roughly align the
 294 models using 4 pairs of corresponding points on each model where the chosen points correspond
 295 to distinct features like hard edges of canals or other structures. These points are used to scale and
 296 rotate the compared model relative to the ground truth data. Once the models are roughly aligned, the
 297 alignment is refined by using an iterative closest point (ICP) algorithm. The ICP algorithm minimizes
 298 the distance between two point clouds by using a mean squared error cost function to estimate the
 299 rotation, translation and scaling that most closely aligns the two point clouds. With the models aligned,
 300 a local quadratic fitting technique is used to determine the distance between each point of the compared
 301 model and the interpolated surface of the ground truth model. This technique is shown in Figure 11.
 302 The cloud to cloud differences are finally fit to a Gaussian distribution and the mean error between the
 303 surfaces is computed (See Table 7). The standard deviation of the error is also computed.

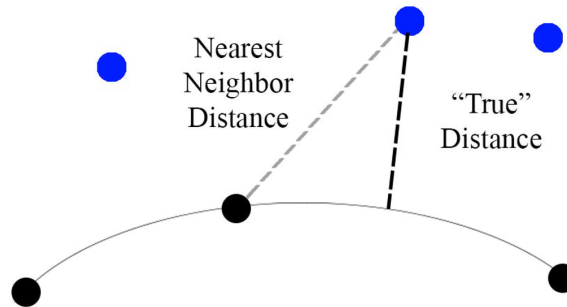
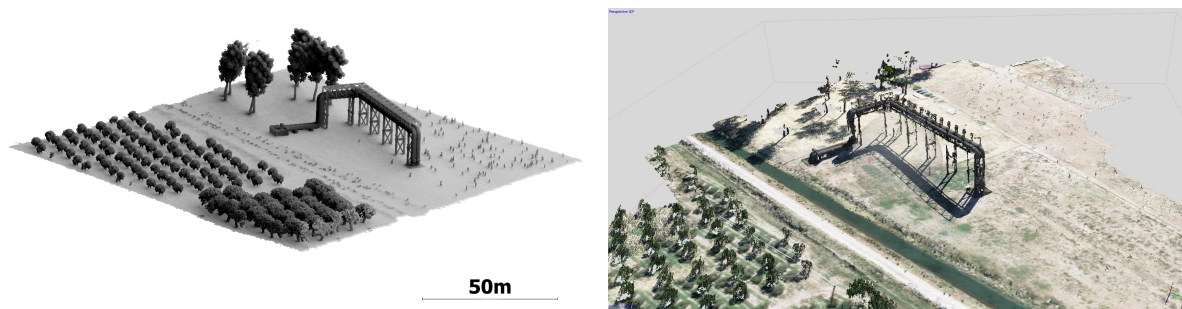


Figure 11. Illustration of the quadratic fitting technique used to find the distance between the reference cloud (black) and the compared cloud (blue).



(a) Ground truth model geometry exported from Terragen. **(b)** Model reconstructed from images in Agisoft Photoscan.

Figure 12. Examples of a ground truth model and a reconstructed model for the piping anomaly location.

304 2.6. Simulated System Implementation

305 Following the collection of simulated images, the physics of each flight is simulated using the
 306 ArduCopter Software-in-the-Loop (SITL) package. The main objective of these simulations is to
 307 compare the flight time required for each path. The optimized flight planner is implemented in Python,

308 and connected to the flight simulation using the 3DR DroneKit library. For these simulations, the
309 desired waypoint navigation speed is set to 60 mph. It is assumed that the UAV platform used has
310 the flight characteristics of a multi-rotor, though for longer endurance it would be preferable to use a
311 larger single-rotor craft or a UAV capable of transitioning between hovering and forward flight.

312 The base flight elevation is set to 90 meters, which corresponds to a 10 cm Ground Sampling
313 Distance (GSD) for an HD video camera. This is done to simulate a two camera multi-scale setup in
314 which most of the long linear feature is captured using lower resolution video, while points of interest
315 are imaged using a higher resolution camera.

316 The UAV is set to fly a path along the one mile canal segment simulated in earlier sections. For
317 this study, optimized flight planning is executed in-flight, however anomaly detection is not performed
318 in real-time, and anomaly locations are marked in advance. When the vehicle reaches each of the
319 pre-defined anomaly locations, the location of the anomaly is passed to the optimized flight planner,
320 and an inspection path is generated in real-time. The UAV then executes this path before continuing
321 with its original flight route. The flight path taken by the UAV can be seen in Figures 14 and 15. The
322 average planning time for each anomaly inspection is approximately 2.3 seconds.

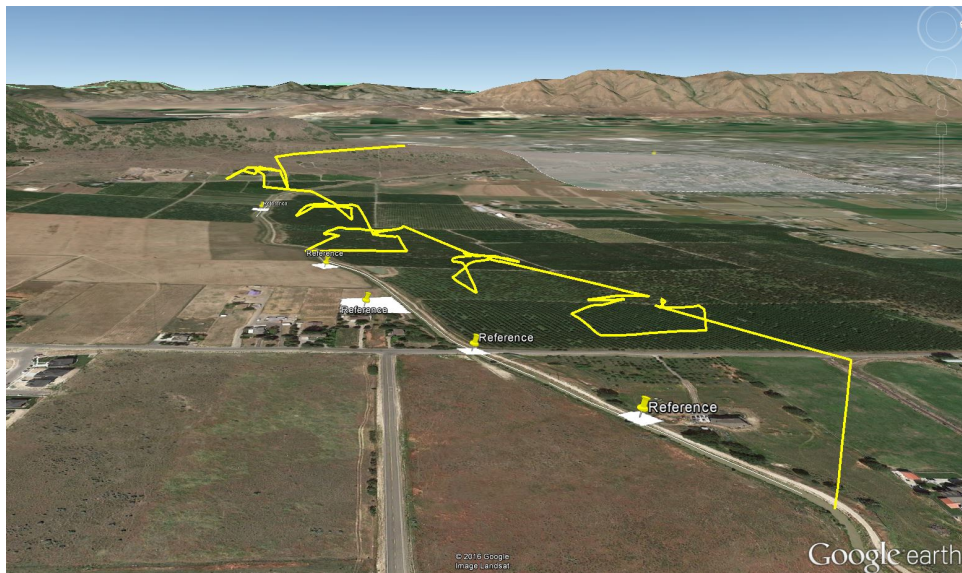


Figure 14. Flight Path simulated along Highline Canal section.

323 To create a baseline for comparison, two additional flights are performed with no anomalies
324 present. The first flight is performed at 20 mph, and provides an upper bound on flight time. The
325 second, at 60 mph provides a lower bound on flight time for the conditions tested.

326 3. Results

327 3.1. 3D Accuracy Testing Results

328 The results of the 3D accuracy testing described in Section 2.5 are shown in Tables 7 and 8. Note
329 that because the flight in Case 1 is relatively close to the ground, the piping is outside the camera field
330 of view, and thus does not appear in the 3D model.

331 As summarized in Figure 16, the average accuracy of the 3D models produced by the multi-scale
332 approach is 11.0 cm. This is much better than the majority of the traditional flights, which average 29.8
333 cm, and is matched only by the low, slow flight of Case 1 with 11.5 cm.

334 An unexpected result from this study is the decrease in accuracy between the single path and the
335 double path, as the double path is expected to be more accurate. The authors believe that this result
336 stems from the setup of the test scene, in which the canal lies directly between the two paths in the

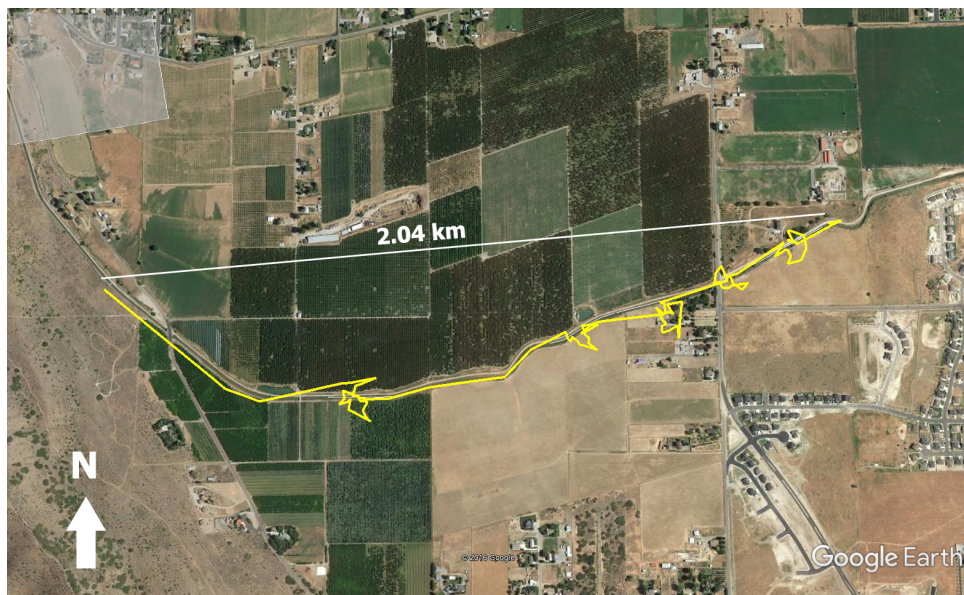


Figure 15. Top view of flight path simulated along Highline Canal section.

Table 7. Mean Accuracy (m)

Site	Case 1	Case 2	Case 3	Case 4	Case 5	Case 6	Case 7	Case 8	Opt
Power	0.15	0.14	0.12	0.22	0.51	0.19	0.48	0.19	0.16
Disc	0.16	0.33	0.12	0.51	0.41	0.15	0.46	0.52	0.08
Pipe	N/A	0.19	0.19	0.57	0.26	0.21	0.4	0.61	0.09
Rail	0.09	0.26	0.15	0.28	0.11	0.21	0.29	0.42	0.10
Slump	0.06	0.31	0.34	0.68	0.13	0.31	0.39	0.69	0.12
Average	0.12	0.25	0.18	0.45	0.28	0.21	0.40	0.49	0.11

Table 8. Standard Deviation (m)

Site	Case 1	Case 2	Case 3	Case 4	Case 5	Case 6	Case 7	Case 8	Opt
Power	0.18	0.15	0.12	0.27	0.37	0.2	0.35	0.23	0.15
Disc	0.18	0.44	0.22	0.79	0.29	0.19	0.39	0.72	0.11
Pipe	N/A	0.03	0.35	0.90	0.27	0.34	0.33	0.81	0.18
Rail	0.02	0.29	0.26	0.28	0.11	0.25	0.27	0.50	0.20
Slump	0.09	0.41	0.48	0.48	0.16	0.39	0.49	0.53	0.19
Average	0.12	0.26	0.29	0.54	0.24	0.27	0.37	0.56	0.17

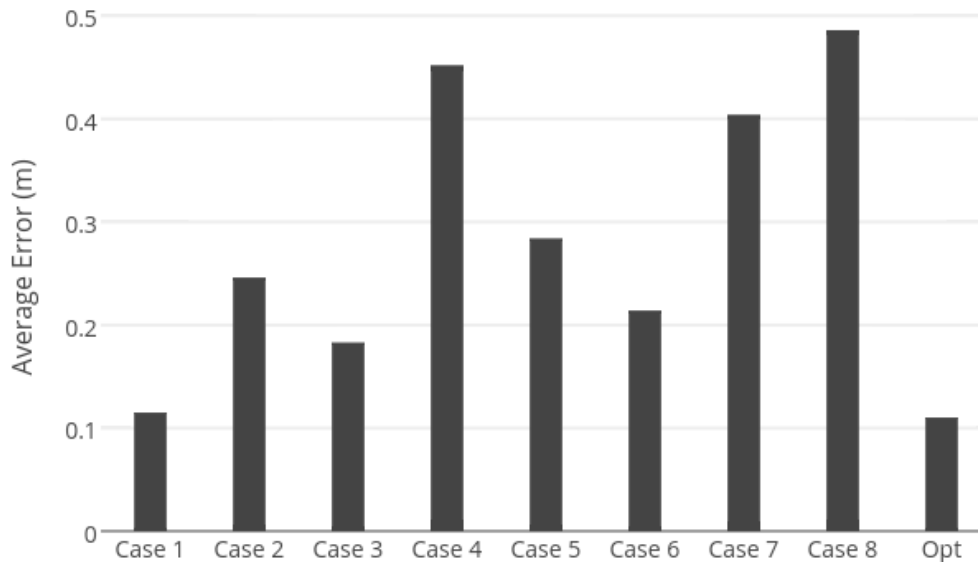


Figure 16. Average Accuracy of 3D Models from Test Cases

337 double path scenario. Terragen uses a realistic lighting model, which includes specular highlighting
 338 and glare on water. The authors believe that the moving highlights and glare on the canal during
 339 the flight make it difficult to match points between the forward and backward path during the 3D
 340 reconstruction, and lead to decreased accuracy. Because the single path cases are flown directly above
 341 the canal, glare is reduced and this problem is avoided. This is illustrated qualitatively in Figure 17
 342 and Figure 18. Figure 17 compares the original geometry of a model segment to the single path and
 343 double path reconstructions. Figure 18 shows a cross section of the canal from one of the double path
 344 models. In both double path cases it can be seen that the model is inaccurate and disjointed at the
 345 canal, supporting the author's conclusions.

346 3.2. Flight Time Results

347 The proposed monitoring system shows improvements over traditional methods in terms of flight
 348 time. Based on the simulated results, the average inspection time per anomaly including planning
 349 and flight time is 1.89 minutes. The flight time savings of this approach scale according to the number
 350 of anomalies detected during the flight. Figure 19 shows the case of a 100 mile flight, comparing
 351 traditional 20 mph and 60 mph monitoring flights to the multi-scale approach. Multi-scale flight times
 352 are calculated by multiplying the average anomaly inspection time by the number of anomalies found
 353 per mile and adding that time to the time required for a baseline 60 mph flight.

354 As Figure 19 shows, flight time savings increase with decreasing anomalies, approaching the
 355 lower limit of the 60 mph flight. One anomaly every five miles produces a 55% savings in flight time
 356 versus the 20 mph case. The break even point, or the point at which a 60 mph flight with inspection
 357 stops takes the same amount of time as a 20 mph flight without stops is 0.67 miles per anomaly.
 358 Combined with the above accuracy testing results, this means that for cases with anomalies spaced

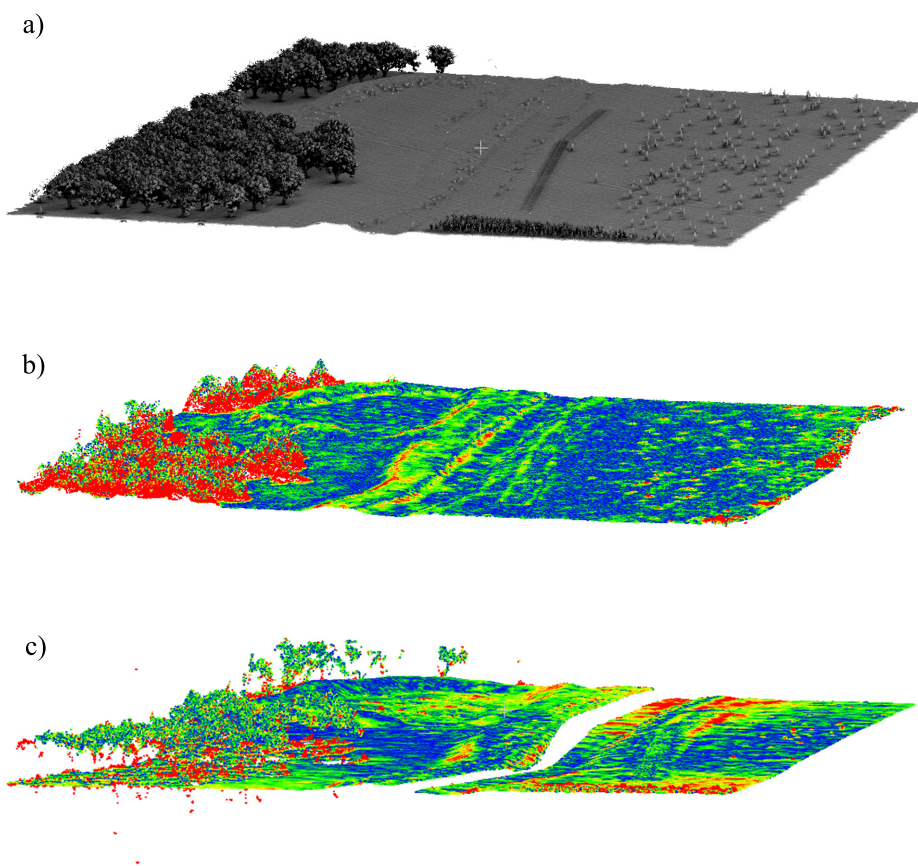


Figure 17. Qualitative comparison of canal models: a) original geometry, b) reconstruction from single path, c) reconstruction from double path. Note the disjoint at the canal surface in the double path case.

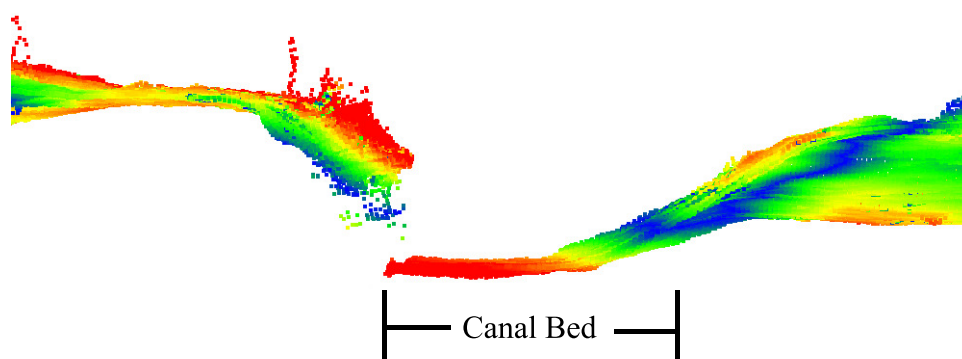


Figure 18. Cross section view of canal from a double path model. Again, the model is seen to be disconnected at the canal surface.

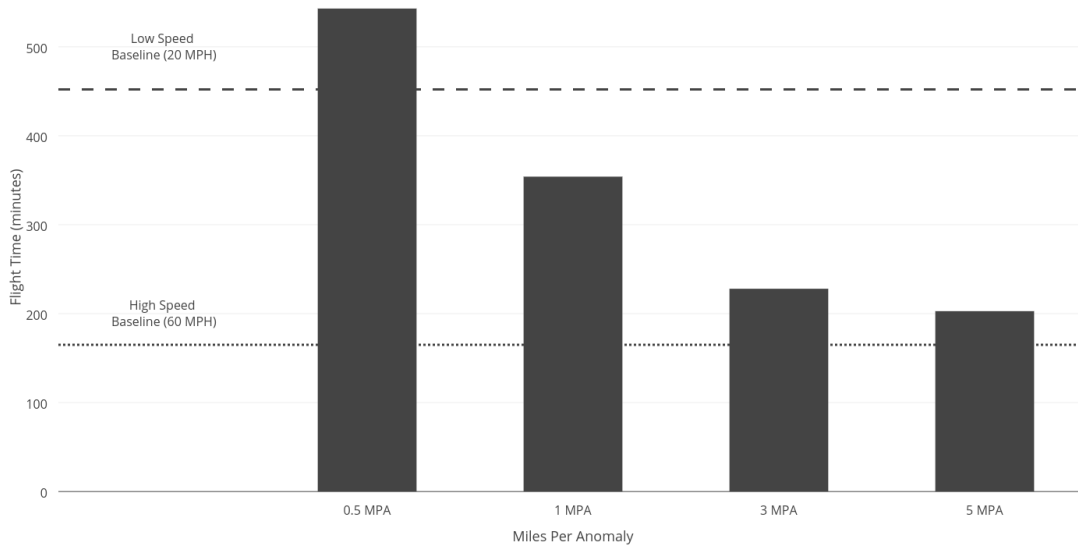


Figure 19. Flight Time Comparison for 100 Mile Flight

359 farther than 0.67 miles apart, the multi-scale approach produces 3D models at the same accuracy as a
 360 low slow flight with less flight time.

361 3.3. Data Quantity Results

362 The proposed methods also show improvement over traditional methods with regards to the
 363 amount of data collected. A major problem with current 3D reconstruction techniques is the large
 364 amount of data generated, which makes viewing, analysis, and storage difficult on a standard
 365 workstation, requiring investments in more powerful computing resources. Reconstruction in
 366 particular scales poorly, with complexity estimates ranging from $O(n^2)$ to $O(n^4)$, where n is the
 367 number of images [43,44].

368 The new method alleviates this problem by focusing data collection and processing power on
 369 infrastructure areas with high information content. High resolution images for 3D reconstruction are
 370 captured only in problem areas, leaving the remainder of the infrastructure to be captured in lower
 371 resolution video for further review if needed. The benefits of this approach in terms of data savings
 372 are expressed in Figure 20.

373 The values in Figure 20 were generated using Equation 4.

$$Data = Miles \cdot \frac{FPM(FO) \cdot M1 + \frac{IPA \cdot M2}{MPA}}{1000} \quad (4)$$

374 This equation describes the gigapixels of imagery collected over a flight using the two camera
 375 setup described above. Here, FPM or Frames Per Mile is the number of HD (1920x1080) video frames
 376 needed per mile to achieve the desired percentage of frame overlap (FO) at the chosen flight speed.
 377 M1 is the number of megapixels per image captured by the HD video camera. MPA is the average
 378 number of Miles Per Anomaly detected. IPA or Images Per Anomaly is the average number of high
 379 resolution images needed per anomaly. M2 is the number of megapixels per image captured by the full
 380 resolution camera. For comparison, Figure 20 also includes the amount of data generated by capturing
 381 full resolution imagery of the entire length of infrastructure during 20 mph and 60 mph flights with
 382 90% overlap. The parameters used to generate Figure 20 are given in Table 9.

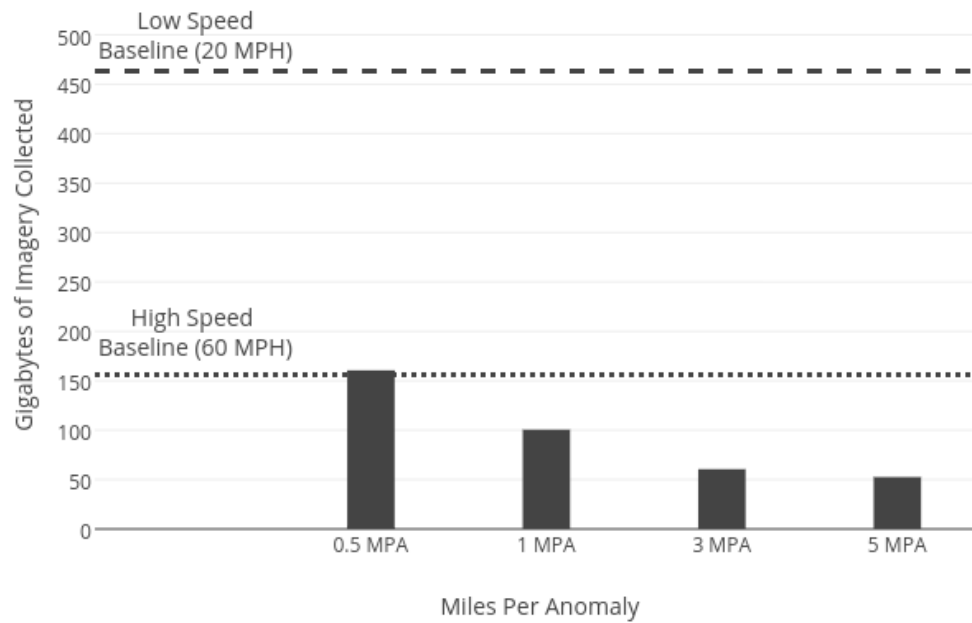


Figure 20. Data Quantity Comparison for 100 Mile Flight

Table 9. Parameter Values used in Equation 4

Parameter	Value
Miles	100
HD Frames-per-Mile (FPM)	193
Desired Frame Overlap (FO)	90%
Camera One Megapixels (M1)	2.1
Average Images-per-Anomaly (IPA)	25
Camera Two Megapixels (M2)	24

383 Together, the results for 3D model accuracy, flight time, and data quantity provide a number of
384 interesting insights. If accurate anomaly detections are possible, the proposed multi-scale infrastructure
385 monitoring approach has the potential to reduce flight times by up to 55% and the quantity of data
386 generated by up to 89% while maintaining accuracy at areas of interest when compared to a low
387 altitude, low speed flight.

388 4. Discussion

389 Much of the research done using UAVs for inspecting long linear infrastructure has focused on
390 using vision to track and follow infrastructure features such as roads and pipelines [22,45,46]. These
391 tracking methods could potentially be combined with the results of this project to create an even more
392 capable system. This project is more similar to the ideas presented in [47], where a network of sensors
393 on an oil pipeline triggers a UAV to investigate an area of possible tampering. In contrast, the method
394 in the the current paper presents the idea of using sensors on-board the UAV itself to trigger flight
395 planning for an area of interest. The view planning algorithm presented is similar to others in the
396 literature [31,48], but as demonstrated provides value when combined with the ideas of anomaly
397 detection and on-board flight planning. This is in contrast to most UAV re-planning literature, where
398 in-flight re-planning is mainly used in exploring unknown environments [49,50].

399 The simulation environment used can be considered both a strength and a limitation of the study.
400 It is a strength because it allows a variety of flight plans and imaging sequences to be constructed
401 and evaluated, which can be difficult in physical tests. It also allows experiments to be conducted in
402 custom environments that can be tailored to test a large combination of specific conditions. However,
403 as no simulation is perfect, this adds the requirement that the results must eventually be validated in
404 physical tests. The authors plan to confirm and extend the results of the study in future real-world
405 flight tests.

406 5. Conclusion

407 This paper proposes a novel method for inspection and monitoring of long linear infrastructure
408 features using UAVs equipped with real-time anomaly detection and in flight re-planning. A simulated
409 test environment is constructed and used to collect synthetic photographs as if taken from UAV
410 flights. A 3D flight planning algorithm suggests sub-optimal but sufficiently accurate waypoints
411 within acceptable CPU time constraints. The procedure and settings used for 3D model reconstruction
412 are also detailed. Standard single and double linear flight paths are compared against the new method
413 in terms of 3D model accuracy, flight time, and the quantity of data collected. A basic demonstration
414 of anomaly detection using a Haar classifier is shown, and additional alternatives discussed.

415 It is shown that compared to a linear flight, the proposed method is able to maintain 3D accuracy
416 at the areas of interest while reducing flight time by up to 55%, and the amount of data generated
417 by up to 89%. This reduces the time required in the field, the image storage required on-board the
418 UAV, and the computer power and storage required for data post processing. These savings reduce
419 the time and cost associated with the monitoring of long linear infrastructure such as pipelines, roads
420 and levees.

421 This paper touches only briefly on the detection of unknown anomalies, instead focusing on
422 quantifying the potential benefits given the assumption such detections are possible. The authors
423 recommend that further work be performed in the area of real-time detection of unknown anomaly
424 detection during UAV flights. Reliable, automatic detection of known objects of interest is valuable.
425 Future work also includes improving the efficiency and effectiveness of the optimized view planning
426 algorithm, and extending it from multi-rotor and single-rotor aircraft to fixed wing platforms. While
427 the simulated environment is useful for identifying general trends, field tests are also needed in the
428 future to validate the simulated results and further explore the details of field implementation. As the
429 simulations in this paper represent a physical location of interest, future field work planned by the
430 authors at that site will be directly comparable to the presented results.

431 **Acknowledgments:** This work was supported by the National Science Foundation Center for Unmanned Aircraft
432 Systems, an Industry/University Cooperative Research Center [Project BYU 13-03: Infrastructure Monitoring].

433 The authors would like to acknowledge the assistance of Spencer Christiansen, Bradley Weber, Kimberly
434 Harris in producing and collecting the data recorded in this paper, as well as their assistance in developing the
435 flight planning algorithms.

436 **Author Contributions:** Abraham Martin conceived and designed the experiments. Landen Blackburn developed
437 the view planning algorithm. Abraham Martin constructed the simulation environment. Abraham Martin
438 performed the experiments and analyzed the results. Joshua Pulsipher assisted in the literature review. John
439 Hedengren and Kevin Franke supervised the project and provided technical input. Abraham Martin, Landen
440 Blackburn, and Joshua Pulsipher wrote the paper with revisions from John Hedengren and Kevin Franke.

441 **Conflicts of Interest**

442 The authors declare no conflict of interest.

443 **References**

- 444 1. Matikainen, L.; Lehtomäki, M.; Ahokas, E.; Hyypä, J.; Karjalainen, M.; Jaakkola, A.; Kukko, A.; Heinonen,
445 T. Remote sensing methods for power line corridor surveys. *ISPRS Journal of Photogrammetry and Remote
446 Sensing* **2016**, *119*, 10 – 31.
- 447 2. Goncalves, J.; Henriques, R. UAV photogrammetry for topographic monitoring of coastal areas. *ISPRS
448 Journal of Photogrammetry and Remote Sensing* **2015**, *104*, 101 – 111.
- 449 3. Martin, R.A.; Hall, A.; Brinton, C.; Franke, K.; Hedengren, J.D. Privacy Aware Mission Planning and Video
450 Masking for UAV Systems. In *AIAA Infotech @ Aerospace*; 2016; p. 0250.
- 451 4. Sankarasrinivasan, S.; Balasubramanian, E.; Karthik, K.; Chandrasekar, U.; Gupta, R. Health Monitoring
452 of Civil Structures with Integrated UAV and Image Processing System. *Procedia Computer Science* **2015**,
453 *54*, 508 – 515.
- 454 5. Pajares, G. Overview and current status of remote sensing applications based on unmanned aerial vehicles
455 (UAVs). *Photogrammetric Engineering & Remote Sensing* **2015**, *81*, 281–329.
- 456 6. Ruggles, S.; Clark, J.; Franke, K.W.; Wolfe, D.; Reimschiessel, B.; Martin, R.A.; Okeson, T.J.; Hedengren,
457 J.D. Comparison of SfM computer vision point clouds of a landslide derived from multiple small UAV
458 platforms and sensors to a TLS-based model. *Journal of Unmanned Vehicle Systems* **2016**, *4*, 1–20.
- 459 7. Palmer, L.M.; Franke, K.W.; Abraham Martin, R.; Sines, B.E.; Rollins, K.M.; Hedengren, J.D. Application
460 and Accuracy of Structure from Motion Computer Vision Models with Full-Scale Geotechnical Field Tests.
461 In *IFCEE 2015*; 2015; pp. 2432–2441.
- 462 8. Franke, K.W.; Rollins, K.M.; Ledezma, C.; Hedengren, J.D.; Wolfe, D.; Ruggles, S.; Bender, C.; Reimschiessel,
463 B. Reconnaissance of Two Liquefaction Sites Using Small Unmanned Aerial Vehicles and Structure
464 from Motion Computer Vision Following the April 1, 2014 Chile Earthquake. *Journal of Geotechnical and
465 Geoenvironmental Engineering* **2016**, p. 04016125.
- 466 9. Colomina, I.; Molina, P. Unmanned aerial systems for photogrammetry and remote sensing: A review.
467 *ISPRS Journal of Photogrammetry and Remote Sensing* **2014**, *92*, 79–97.
- 468 10. Westoby, M.; Brasington, J.; Glasser, N.; Hambrey, M.; Reynolds, J. ‘Structure-from-Motion’
469 photogrammetry: A low-cost, effective tool for geoscience applications. *Geomorphology* **2012**, *179*, 300–314.
- 470 11. Saadatseresht, M.; Hashempour, A.; Hasanlou, M. UAV Photogrammetry: a Practical Solution for
471 Challenging Mapping Projects. *The International Archives of Photogrammetry, Remote Sensing and Spatial
472 Information Sciences* **2015**, *40*, 619.
- 473 12. Fytilis, A.L.; Prokos, A.; Koutroumbas, K.D.; Michail, D.; Kontoes, C.C. A methodology for near real-time
474 change detection between Unmanned Aerial Vehicle and wide area satellite images. *ISPRS Journal of
475 Photogrammetry and Remote Sensing* **2016**, *119*, 165 – 186.
- 476 13. Ruf, B.; Schuchert, T. Towards real-time change detection in videos based on existing 3D models. 2016, Vol.
477 10004, p. 100041H.
- 478 14. Shi, J.; Wang, J.; Xu, Y. Object-based change detection using georeferenced UAV images. *Int. Arch.
479 Photogramm. Remote Sens. Spat. Inf. Sci* **2011**, *38*, 177–182.
- 480 15. Sun, L.; Castagno, J.; Hedengren, J.; Beard, R. Parameter estimation for towed cable systems using moving
481 horizon estimation. *Aerospace and Electronic Systems, IEEE Transactions on* **2015**, *51*, 1432–1446.

- 482 16. Kamate, S.; Yilmazer, N. Application of Object Detection and Tracking Techniques for Unmanned Aerial
483 Vehicles. *Procedia Computer Science* **2015**, *61*, 436–441.
- 484 17. Gleason, J.; Nefian, A.V.; Bouyssounousse, X.; Fong, T.; Bebis, G. Vehicle detection from aerial imagery.
485 *2011 IEEE International Conference on Robotics and Automation* **2011**, *2*, 2065–2070.
- 486 18. Krizhevsky, A.; Sutskever, I.; Hinton, G.E. Imagenet classification with deep convolutional neural networks.
487 *Advances in neural information processing systems*, 2012, pp. 1097–1105.
- 488 19. Máthé, K.; Buşoniu, L. Vision and control for UAVs: A survey of general methods and of inexpensive
489 platforms for infrastructure inspection. *Sensors* **2015**, *15*, 14887–14916.
- 490 20. Hausamann, D.; Zirnig, W.; Schreier, G.; Strobl, P. Monitoring of gas pipelines—a civil UAV application.
491 *Aircraft Engineering and Aerospace Technology* **2005**, *77*, 352–360.
- 492 21. Zhang, J.; Liu, L.; Wang, B.; Chen, X.; Wang, Q.; Zheng, T. High speed automatic power line detection and
493 tracking for a UAV-based inspection. *Proceedings of the 2012 International Conference on Industrial Control and*
494 *Electronics Engineering, ICICEE 2012* **2012**, pp. 266–269.
- 495 22. Rathinam, S.; Kim, Z.W.; Sengupta, R. Vision-based monitoring of locally linear structures using an
496 unmanned aerial vehicle 1. *Journal of Infrastructure Systems* **2008**, *14*, 52–63.
- 497 23. Zhou, H.; Kong, H.; Wei, L.; Creighton, D.; Nahavandi, S. Efficient road detection and tracking for
498 unmanned aerial vehicle. *IEEE Transactions on Intelligent Transportation Systems* **2015**, *16*, 297–309.
- 499 24. Chen, S.; Li, Y.; Kwok, N.M. Active vision in robotic systems: A survey of recent developments. *The*
500 *International Journal of Robotics Research* **2011**, *30*, 1343–1377.
- 501 25. Zhao, J.; Cheung, S.C.S. Optimal visual sensor planning. *Proceedings - IEEE International Symposium on*
502 *Circuits and Systems* **2009**, pp. 165–168.
- 503 26. Chen, S.Y.; Li, Y.F. Automatic Sensor Placement for Model-Based Robot Vision. *IEEE Transactions on*
504 *Systems, Man, and Cybernetics, Part B: Cybernetics* **2004**, *34*, 393–408.
- 505 27. Siebert, S.; Teizer, J. Mobile 3D mapping for surveying earthwork projects using an Unmanned Aerial
506 Vehicle (UAV) system. *Automation in Construction* **2014**, *41*, 1–14.
- 507 28. Van Leeuwen, J.; Leeuwen, J. *Handbook of Theoretical Computer Science: Algorithms and complexity*; Elsevier,
508 1994.
- 509 29. Saadat, S.M.; Samadzadegan, F. Multi-objective optimization of vision metrology camera placement based
510 on Pareto front concept by NSGA-II method **2008**.
- 511 30. Papachristos, C.; Alexis, K.; Carrillo, L.R.G.; Tzes, A. Distributed infrastructure inspection path planning
512 for aerial robotics subject to time constraints. *Unmanned Aircraft Systems (ICUAS), 2016 International*
513 *Conference on. IEEE, 2016*, pp. 406–412.
- 514 31. Hoppe, C.; Wendel, A.; Zollmann, S.; Pirker, K.; Irschara, A.; Bischof, H.; Kluckner, S. Photogrammetric
515 camera network design for micro aerial vehicles. *Computer vision winter workshop (CVWW), 2012, Vol. 8*,
516 pp. 1–3.
- 517 32. Sun, L.; Hedengren, J.D.; Beard, R.W. Optimal Trajectory Generation using Model Predictive Control for
518 Aerially Towed Cable Systems. *Journal of Guidance, Control, and Dynamics* **2014**, *37*, 525–539.
- 519 33. Piatti, E.J.; Lerma, J.L. Virtual Worlds for Photogrammetric Image-Based Simulation and Learning.
520 *Photogrammetric Record* **2013**, *28*, 27–42.
- 521 34. James, M.R.; Robson, S. Mitigating systematic error in topographic models derived from UAV and
522 ground-based image networks. *Earth Surface Processes and Landforms* **2014**, *39*, 1413–1420.
- 523 35. Saur, G.; Bartelsen, J. Experimental application of simulation tools for evaluating UAV video change
524 detection. *SPIE Security+ Defence. International Society for Optics and Photonics, 2015*, p. 96530P.
- 525 36. Martin, R.; Rojas, I.; Franke, K.; Hedengren, J. Evolutionary View Planning for Optimized UAV Terrain
526 Modeling in a Simulated Environment. *Remote Sensing* **2015**, *8*, 26.
- 527 37. Pix4D. Designing the Images Acquisition Plan. [https://support.pix4d.com/hc/en-us/articles/202557459-](https://support.pix4d.com/hc/en-us/articles/202557459-Step-1-Before-Starting-a-Project-1-Designing-the-Images-Acquisition-Plan-a-Selecting-the-Images-Acquisition-Plan-Type)
528 [Step-1-Before-Starting-a-Project-1-Designing-the-Images-Acquisition-Plan-a-Selecting-the-Images-](https://support.pix4d.com/hc/en-us/articles/202557459-Step-1-Before-Starting-a-Project-1-Designing-the-Images-Acquisition-Plan-a-Selecting-the-Images-Acquisition-Plan-Type)
529 [Acquisition-Plan-Type](https://support.pix4d.com/hc/en-us/articles/202557459-Step-1-Before-Starting-a-Project-1-Designing-the-Images-Acquisition-Plan-a-Selecting-the-Images-Acquisition-Plan-Type), 2016. Accessed: 2016-06-15.
- 530 38. Scott, W.R. Model-based view planning. *Machine Vision and Applications* **2009**, *20*, 47–69.
- 531 39. Chekuri, C.; Clarkson, K.L.; Har-Peled, S. On the Set Multi-cover Problem in Geometric Settings.
532 *Proceedings of the Twenty-fifth Annual Symposium on Computational Geometry*; ACM: New York,
533 NY, USA, 2009; SCG '09, pp. 341–350.

- 534 40. Christofides, N. Worst-case analysis of a new heuristic for the travelling salesman problem. Technical
535 report, DTIC Document, 1976.
- 536 41. Agisoft. Agisoft PhotoScan Professional Edition. <http://www.agisoft.ru/products/photoscan>, 2014.
537 Accessed: 2016-06-15.
- 538 42. CloudCompare. CloudCompare. <http://cloudcompare.org/>, 2016. Accessed: 2016-07-12.
- 539 43. Wu, C. Towards Linear-time Incremental Structure from Motion. *2013 International Conference on 3D Vision*
540 **2013**, pp. 127–134.
- 541 44. Pieterse, V.; Black, P.E. big-O notation, 2016.
- 542 45. Bruggemann, T.S.; Ford, J.J.; Walker, R.A. Control of Aircraft for Inspection of Linear Infrastructure. *IEEE*
543 *Transactions on Control Systems Technology* **2011**, *19*, 1397–1409.
- 544 46. Sharma, H.; Dutta, T.; Adithya, V.; Balamuralidhar, P. A Real-Time Framework for Detection of Long
545 Linear Infrastructural Objects in Aerial Imagery; Springer, Cham, 2015; pp. 71–81.
- 546 47. Abayomi, E.; Ayo, D.; Omowunmi, O. Above - Ground Pipeline Monitoring and Surveillance Drone
547 Reactive To Attacks. 3rd International Conference on African Development Issues, 2016.
- 548 48. Bircher, A.; Kamel, M.; Alexis, K.; Burri, M.; Oettershagen, P.; Omari, S.; Mantel, T.; Siegwart, R.
549 Three-dimensional coverage path planning via viewpoint resampling and tour optimization for aerial
550 robots. *Autonomous Robots* **2016**, *40*, 1059–1078.
- 551 49. Xue, Q.; Cheng, P.; Cheng, N. Offline path planning and online replanning of UAVs in complex terrain.
552 Proceedings of 2014 IEEE Chinese Guidance, Navigation and Control Conference. IEEE, 2014, pp.
553 2287–2292.
- 554 50. Oleynikova, H.; Burri, M.; Taylor, Z.; Nieto, J.; Siegwart, R.; Galceran, E. Continuous-time trajectory
555 optimization for online UAV replanning. 2016 IEEE/RSJ International Conference on Intelligent Robots
556 and Systems (IROS). IEEE, 2016, pp. 5332–5339.

557 © 2017 by the authors. Submitted to *Remote Sens.* for possible open access publication
558 under the terms and conditions of the Creative Commons Attribution (CC BY) license
559 (<http://creativecommons.org/licenses/by/4.0/>).